micromachines

*Article*

# Geometrical Optimization and Transverse Thermoelectric Performances of Fe/$Bi_2Te_{2.7}Se_{0.3}$ Artificially Tilted Multilayer Thermoelectric Devices

**Hongyu Zhou *, Huang Liu, Guoping Qian *, Huanan Yu, Xiangbing Gong, Xi Li and Jianlong Zheng**

National Engineering Laboratory for Highway Maintenance Technology, School of Traffic and Transportation Engineering, Changsha University of Science and Technology, Changsha 410114, China; lhcsust@163.com (H.L.); huanan.yu@csust.edu.cn (H.Y.); xbgong@csust.edu.cn (X.G.); csu_lixi@126.com (X.L.); zjl@csust.edu.cn (J.Z.)
* Correspondence: zhouhongyu23@126.com (H.Z.); guopingqian@sina.com (G.Q.)

**Abstract:** Transverse thermoelectric performance of the artificially tilted multilayer thermoelectric device (ATMTD) is very difficult to be optimized, due to the large degree freedom in device design. Herein, an ATMTD with Fe and $Bi_2Te_{2.7}Se_{0.3}$ (BTS) materials was proposed and fabricated. Through high-throughput calculation of Fe/BTS ATMTD, a maximum of calculated transverse thermoelectric figure of merit of 0.15 was obtained at a thickness ratio of 0.49 and a tilted angle of 14°. For fabricated ATMTD, the whole Fe/BTS interface is closely connected with a slight interfacial reaction. The optimizing Fe/BTS ATMTD with 12 mm in length, 6 mm in width and 4 mm in height has a maximum output power of 3.87 mW under a temperature difference of 39.6 K. Moreover the related power density per heat-transfer area reaches 53.75 $W \cdot m^{-2}$. This work demonstrates the performance of Fe/BTS ATMTD, allowing a better understanding of the potential in micro-scaled devices.

**Keywords:** Fe/$Bi_2Te_{2.7}Se_{0.3}$; rational design; transverse thermoelectric performances

check for updates

**Citation:** Zhou, H.; Liu, H.; Qian, G.; Yu, H.; Gong, X.; Li, X.; Zheng, J. Geometrical Optimization and Transverse Thermoelectric Performances of Fe/$Bi_2Te_{2.7}Se_{0.3}$ Artificially Tilted Multilayer Thermoelectric Devices. *Micromachines* **2022**, *13*, 233. https://doi.org/10.3390/mi13020233

Academic Editor: Aiqun Liu

Received: 31 December 2021
Accepted: 28 January 2022
Published: 30 January 2022



## 1. Introduction

Thermoelectric (TE) technology is well-known for its capability to directly convert heat into electricity, and it has a great value in power generation, cooling, thermal detection, etc. [1–3]. The performance of TE technology is determined by the figure of merit (ZT) [4]. Over the past two decades, great advancements, including band-structure engineering [5–7], phonon engineering [8–11] and magnetoelectric engineering [12,13], have been proposed to enhance the ZT values of traditional TE materials. Nevertheless, the parallel or anti-parallel relationship between the electrical current (I) and the heat flow (Q) impedes the progress of optimizing the transport parameters in an individual way to the higher ZT values. Beyond that, the traditional TE devices perform complex π-type structure. Multiple n-type TE legs and p-type TE legs are connected electrically in series through metal electrodes to enlarge the TE electromotive force, thus hindering their miniaturization to meet the requirements of microelectronic applications [14,15].

Transverse TE counterparts have been proposed as an alternative approach, whereby it can generate off-diagonal element I and Q [16,17]. The I and Q are perpendicular to one another; the electrical conductivity, thermal conductivity, and Seebeck coefficient are anisotropic. It brings three distinct advantages. First, there is a greater degree of freedom in optimizing the transport parameters in an individual way. Second, the related transverse TE device is single-leg, and no electrode required. It can be cut into a variety of shapes, such as tubes, sheets, thin film, trapezoid, and cone, to fit the demand of infinite-stage cascade power generator or cooler [18–20]. Third, the dependence of $V_x$ on the length to height ratio is greatly beneficial in developing the micro/nano-scaled devices. It works best for the extremely long and thin device [21–24].

One of the transverse TE counterparts, the artificially tilted multilayer thermoelectric device (ATMTD), has gained increasing attention, because, in addition to the three distinct advantages above, the artificial combination can be almost any material [25,26]. This gives more options to explore the high-performance ATMTD. To establish the off-diagonal element, both combinatorial materials in the ATMTD must be stacked together in an alternating pattern and then turned at a tilted angle (θ) to be effective in the anisotropic Seebeck coefficient. The thickness ratio (δ) of each combinatorial material also makes its own contribution to the anisotropy of electrical and thermal conductivity. The concerned performance of the transverse figure of merit ($ZT_{zx}$) in ATMTD is defined as $ZT_{zx} = \sigma_{xx}S_{zx}^2T/\kappa_{zz}$, where the $ZT_{zx}$, $\sigma_{xx}$, $S_{zx}$, $\kappa_{zz}$ and T are the transverse figure of merit, transverse electrical conductivity, transverse Seebeck coefficient, transverse thermal conductivity and absolute temperature, respectively [27]. Recently, many efforts have been made to combine different materials to study the $ZT_{zx}$ of ATMTD, such as Al/Si [28], Bi/Cu [29], Pb/$Bi_2Te_3$ [30], Ni/$Bi_{0.5}Sb_{1.5}Te_3$ [31–33], $YbAl_3$/$Bi_{0.5}Sb_{1.5}Te_3$ [34] and Bi/$Bi_{0.5}Sb_{1.5}Te_3$ [24]. However, the geometrical configurations (θ and δ) of the ATMTD also play a very important role in improvement of $ZT_{zx}$, since it takes advantage of the transverse TE effect in an artificially tilted multilayer structure. A rational design for the given combinations that guides the $ZT_{zx}$ optimization is highly desired.

In this study, n-type $Bi_2Te_{2.7}Se_{0.3}$ (BTS) and p-type pure irons (Fe) were selected as the combinatorial materials for a new ATMTD. Because BTS has a large Seebeck coefficient, small electrical and thermal conductivities near room temperature, Fe has a small Seebeck coefficient, large electrical and thermal conductivities [35]. The large different values for TE parameters in BTS and Fe are beneficial to its $ZT_{zx}$ [36]. To exploit the best geometrical configurations of the given Fe/BTS ATMTD, a high-throughput calculation was performed. A Fe/BTS ATMTD of 12 mm in length, 6 mm in width and 4 mm in height was fabricated with the optimized tilted angle of 14° and optimized thickness ratio of 0.49. The results reveal that the experimental $S_{zx}$ value is in good agreement with theoretical ones. The maximum output power and related power density per heat-transfer area are about 3.87 mW and 53.75 $Wm^{-2}$ under a temperature difference of 39.6 K, respectively.

## 2. Methods of Calculation and Experiment

### *2.1. Theoretical Calculation Model of Fe/BTS ATMTD*

The structure of ATMTD contains two alternately stacked layers, Fe and BTS, with thickness $d_{Fe}$ and $d_{BTS}$. After the stacking layer plane is tilted at an angle, θ, against the ATMTD surface ($\theta \neq 0°$ or 90°), the anisotropy of transport parameters comes from two alternately stacked layers, parallel and perpendicular stacking-layer planes, as well as tilt. This means that the Seebeck coefficient of Fe/BTS ATMTD is anisotropic and the off-diagonal Seebeck coefficient of Fe/BTS ATMTD is non-zero, which provides the theoretical background to see transverse TE effect. As shown in Figure 1, when a temperature gradient ($\Delta T_z$) in Fe/BTS ATMTD is established along the *z*-axis under the hot-side temperature ($T_H$) and cold-side temperature ($T_C$), it will yield a transverse TE electromotive force ($\Delta V_x$) along the *x*-axis. The $\Delta V_x$ can be expressed as follows:

$$\Delta V_x = S_{zx}\Delta T_z l/h \quad (1)$$

where l and h are the length and the height of Fe/BTS ATMTD, respectively; and $S_{zx}$ is the difference of Seebeck coefficient in the *z*-axis and *x*-axis direction of Fe/BTS ATMTD.

The $\Delta V_x$ and other TE performance of Fe/BTS ATMTD are relevant to $ZT_{zx} = \sigma_{xx}S_{zx}^2T/\kappa_{zz}$. To maximum $ZT_{zx}$ values, we begin with a description of the off-diagonal elements ($\rho_{xx}$, $\kappa_{zz}$, and $S_{zx}$) along the different directions. It can be described by the tensors (M):

$$[M] = \begin{bmatrix} M_{//}\cos^2\theta + M_{\perp}\sin^2\theta & 0 & (M_{//} - M_{\perp})\sin\theta\cos\theta \\ 0 & M_{//} & 0 \\ (M_{//} - M_{\perp})\sin\theta\cos\theta & 0 & M_{//}\sin^2\theta + M_{\perp}\cos^2\theta \end{bmatrix} \quad (2)$$

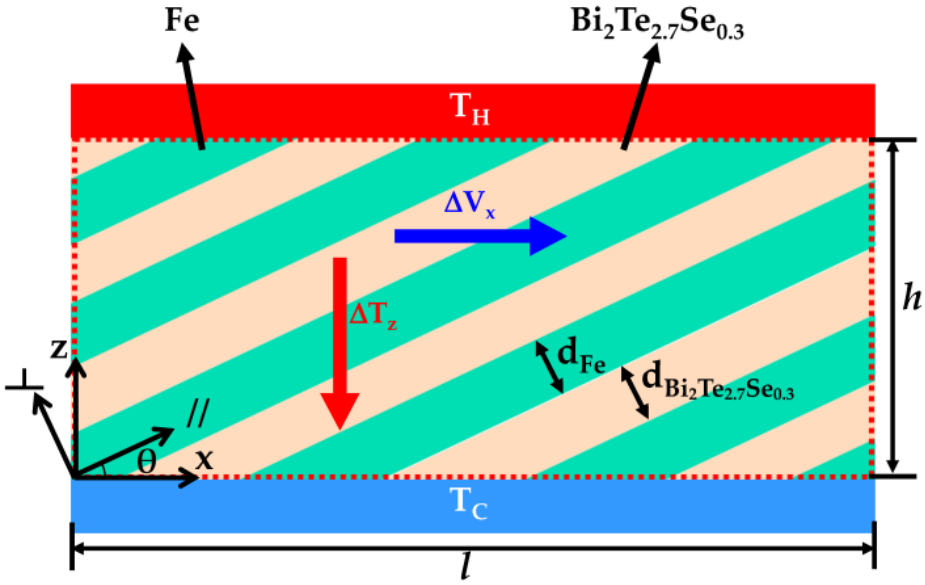


**Figure 1.** Simplified model of the Fe/BTS ATMTD from the sectional view.

Then, the $\sigma_{xx}$, $\kappa_{zz}$ and $S_{zx}$ can be given as a function with tilted angle, θ, of the stacking layer plane in Fe/BTS ATMTD, which includes $\sigma_{//}$, $\sigma_{\perp}$, $S_{//}$, S, $\kappa_{//}$, $\kappa_{\perp}$ and θ.

$$\sigma_{xx} = 1/\rho_{xx} = 1/(\rho_{//}\cos^2\theta + \rho_{\perp}\sin^2\theta) = \sigma_{//}\sigma_{\perp}/(\sigma_{\perp}\cos^2\theta + \sigma_{//}\sin^2\theta) \quad (3)$$

$$S_{zx} = (S_{//} - S_{\perp})\sin\theta\cos\theta \quad (4)$$

$$\kappa_{zz} = \kappa_{//}\sin^2\theta + \kappa_{\perp}\cos^2\theta \quad (5)$$

To illustrate how transport behaviors arise in alternately stacked layers, we considered the simplified model below. Assume that the electrical and thermal contact resistances in the Fe/BTS ATMTD could be ignored. Combined with Kirchhoff's theory [28], the electrical conductivity ($\sigma_{//}$, $\sigma_{\perp}$), Seebeck coefficient ($S_{//}$, $S_{\perp}$) and thermal conductivity ($\kappa_{//}$, $\kappa_{\perp}$) parallel and perpendicular to the stacking layer plane become as follows:

$$\sigma_{//} = \delta\sigma_{Fe} + (1-\delta)\sigma_{BTS},\ \sigma_{\perp} = \sigma_{Fe}\sigma_{BTS}/[(1-\delta)\sigma_{Fe} + \delta\sigma_{BTS}] \quad (6)$$

$$S_{//} = [\delta S_{Fe}\sigma_{Fe} + (1-\delta)S_{BTS}\sigma_{BTS}]/[\delta\sigma_{Fe} + (1-\delta)\sigma_{BTS}] \quad (7)$$

$$S_{\perp} = [\delta S_{Fe}\kappa_{BTS}) + (1-\delta)S_{BTS}\kappa_{Fe}]/[(1-\delta)\kappa_{Fe} + \delta\kappa_{BTS}) \quad (8)$$

$$\kappa_{//} = \delta\kappa_{Fe} + (1-\delta)\kappa_{BTS},\ \kappa_{\perp} = \kappa_{Fe}\kappa_{BTS}/[(1-\delta)\kappa_{Fe} + \delta\kappa_{BTS}] \quad (9)$$

where the subscripts "//" and "$_{\perp}$" denote the directions parallel and perpendicular to the stacking layer plane of the Fe/BTS ATMTD. Moreover, $\sigma_{Fe}$, $\sigma_{BTS}$, $S_{Fe}$, $S_{BTS}$, $\kappa_{Fe}$ and $\kappa_{BTS}$ are the electrical conductivity of Fe, electrical conductivity of BTS, Seebeck coefficient of Fe, Seebeck coefficient of BTS, thermal conductivity of Fe and thermal conductivity of BTS, respectively; and $\delta = d_{Fe}/(d_{Fe} + d_{BTS})$ represents the thickness ratio of Fe layer in Fe/BTS ATMTD.

Note that both the TE parameter ($\sigma_{Fe}$, $\sigma_{BTS}$, $S_{Fe}$, $S_{BTS}$, $\kappa_{Fe}$ and $\kappa_{BTS}$) of constituent materials and the geometrical configuration (δ and θ) of Fe/BTS ATMTD are the key factor to maximum $ZT_{zx}$ values. The solution for $ZT_{zx}$ is complex. A high-throughput calculation to investigate the relevance between the transverse TE properties is very important.

### *2.2. Experimental Procedure of Fabricated Fe/BTS ATMTD*

The Fe/BTS ATMTD was fabricated by using spark plasma sintering (SPS) and two-step wire-cut electrical discharge machining (WEDM) method. The specific processes are presented in Figure 2. Firstly, it was necessary to optimize the geometrical configuration (δ

and θ) of Fe/BTS ATMTD with theoretical calculation before its manufacture to maximize $ZT_{zx}$ value. Secondly, the starting materials, including the Fe wafers and BTS powders, were alternately loaded in graphite die. The thicknesses of layers Fe and BTS were identical to the designed δ value. Thirdly, the alternately stacked material was sintered into a multilayer cylinder by SPS at 673 K for 10 min, under a pressure of 40 MPa. Fourthly, the multilayer cylinder was shaped into an artificially tilted multilayer block, and the cutting position was controlled by the two-step WEDM method to realize the desired θ value. Finally, the Fe/BTS ATMTD with the optimized δ and θ was obtained via soldering Cu wires and bonding $Al_2O_3$ ceramic plates on the artificially tilted multilayer block.

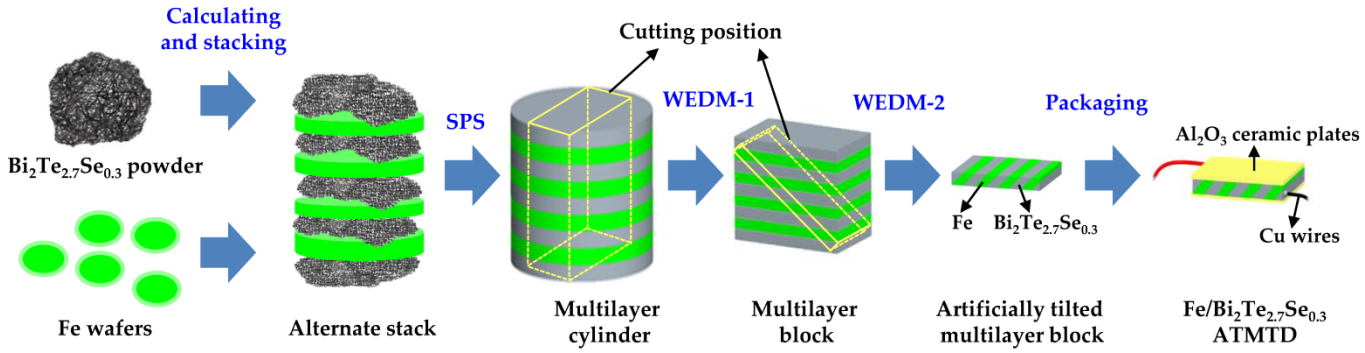


**Figure 2.** Sketch map of the processes of fabricated Fe/BTS ATMTD.

### *2.3. Characterization and Performance Evaluation of Fe/BTS ATMTD*

The microstructure and element distribution at the interface were characterized by electron probe microanalysis (EPMA, JEOL JXA-8230) equipped with an X-ray spectroscopy detector. The power generation performance of Fe/BTS ATMTD was evaluated at a temperature difference from 10 to 40 K, using a self-made measuring equipment that was presented in our previous report [33,34].

## 3. Results and Discussion

### *3.1. Geometrical Configuration Determination of Fe/BTS ATMTD*

To quickly screen the maximum $ZT_{zx}$ from a large number of combinations from δ and θ, a high-throughput calculation for $\sigma_{xx}$, $S_{zx}$, $\kappa_{zz}$ and $ZT_{zx}$ was implemented under different δ and θ values. The room-temperature electrical conductivity (σ), Seebeck coefficient (S), and thermal conductivity (κ) of Fe and BTS in the calculation model refer to Table 1.

**Table 1.** Room-temperature transport parameters of Fe and BTS.

| Materials | σ ($10^5$ S·m$^{-1}$) | S (μ·V·K$^{-1}$) | κ (W·m$^{-1}$·K$^{-1}$) |
|---|---|---|---|
| Fe | 99 [a] | 15.0 [b] | 80.4 [a] |
| BTS | 1.4 [a] | −122.1 [a] | 1.3 [a] |

[a] Experimentally obtained by authors. [b] Reference [37].

Figure 3 shows the contour maps of Fe/BTS as a function of δ and θ. It can be seen that the $\sigma_{xx}$ gradually increases with increasing the δ value from 0 to 1, due to the increased thickness of high conductivity Fe layer in Fe/BTS ATMTD (Figure 3a). Moreover, $\sigma_{xx}$ first decreases slowly when θ value is less than 20° and then decreases dramatically in the range of 20–90°. This reduction indicates that the small θ can enhance the electron transport of Fe/BTS ATMTD in the *x*-axis direction. Figure 3b shows the δ and θ dependence on the $S_{zx}$. The positive $S_{zx}$ values indicate a p-type conduction behavior of Fe/BTS ATMTD. With increasing the δ, $S_{zx}$ first increases and then decreases. When the δ value is close to 0.5, a larger $S_{zx}$ value can be found. $S_{zx}$ increases slowly when θ value is less than 30°, and then increases dramatically in the range of 30–45°. Nevertheless, when the θ value is larger than 45°, a drop of $S_{zx}$ occurs. The maximum $S_{zx}$ value of 66.3 μVK$^{-1}$ is obtained at δ = 0.48 and

θ = 45°. Figure 3c displays the δ and θ dependence of the $\kappa_{zz}$. The $\kappa_{zz}$ gradually increases with increasing the δ. In contrast to $\sigma_{xx}$, the $\kappa_{zz}$ gradually increases with increasing the θ, meaning that the small θ will be reduced the thermal transport of Fe/BTS ATMTD in the *z*-axis direction. Thus, a choice of small θ is confirmed to simultaneously optimize electrical and thermal transport properties in Fe/BTS ATMTD. Figure 3d shows the δ and θ dependence of the $ZT_{zx}$. By increasing the δ and θ, the $ZT_{zx}$ value first increases and then decreases. The maximum $ZT_{zx}$ value for Fe/BTS ATMTD is 0.15 with δ = 0.49 and θ = 14°, which is increased by 400% as compared with that with δ = 0.48 and θ = 45°. Therefore, a properly geometrical configuration is favorable for maximizing the $ZT_{zx}$ value in the ATMTD.

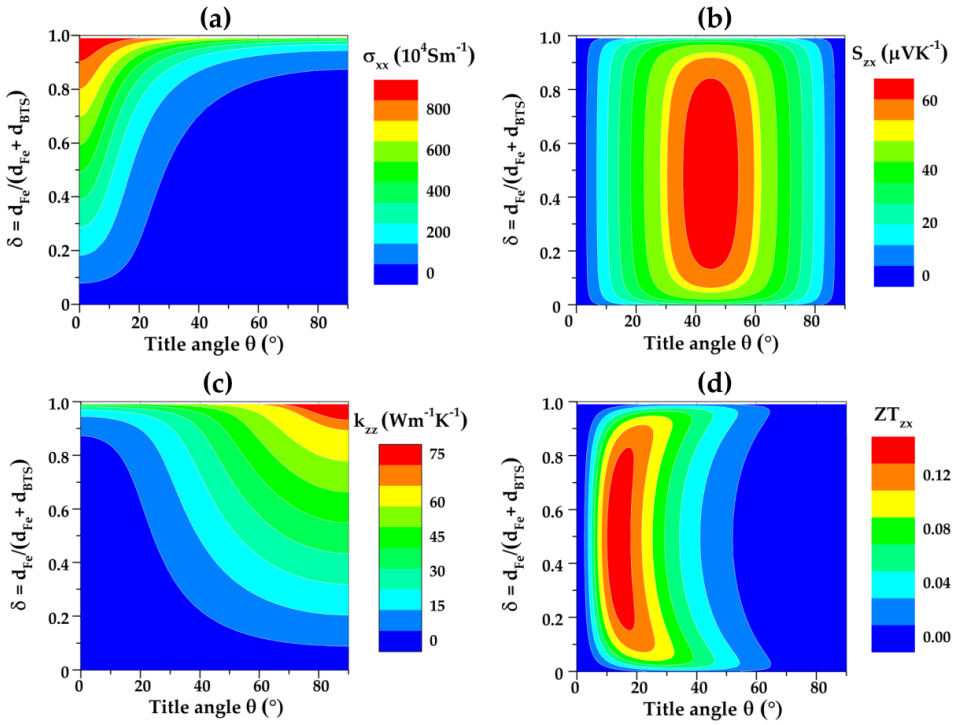


**Figure 3.** Thickness ratio (δ) and tilted angle (θ) dependences of (**a**) electrical conductivity $\sigma_{xx}$; (**b**) transverse Seebeck coefficient $S_{zx}$; (**c**) thermal conductivity $\kappa_{zz}$; and (**d**) transverse figure of merit $ZT_{zx}$ of Fe/BTS ATMTD.

### *3.2. Microstructure Characterization of Fe/BTS ATMTD*

Based on the optimized δ and θ given by the high-throughput calculations, a packaged Fe/BTS ATMTD was fabricated (Figure 4a). The Fe/BTS ATMTD is rectangular, which is 12 mm in length, 6 mm in width and 4 mm in height. Figure 4b shows the cross-sectional image of artificially tilted multilayer block. The bright areas are Fe, while the black ones are BTS. The cross-sections with 10 alternately stacked layers of Fe and BTS are clearly visible. The whole Fe/BTS artificially tilted multilayer block is closely connected without macro-cracks. The thicknesses of Fe and BT layers are 1 mm and 1.04 mm, respectively, thus indicating that the δ value is 0.49. The as-prepared θ value is 14°. The as-prepared δ and θ values are consistent with the desired geometrical configuration.

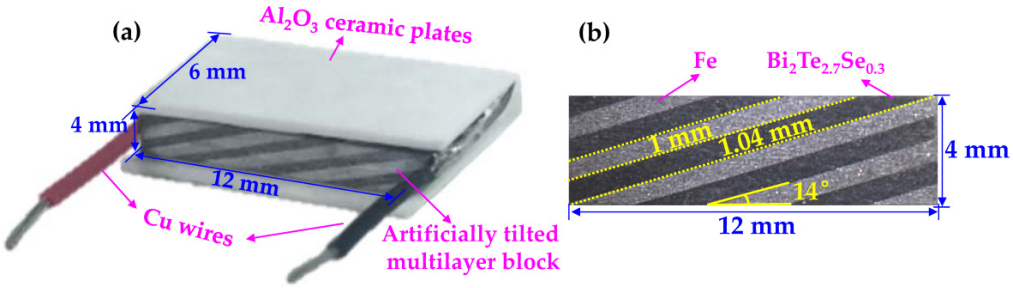


**Figure 4.** (**a**) Packaged Fe/BTS ATMTD; (**b**) cross-sectional image of artificially tilted multilayer block.

Figure 5a presents a backscattered electron image (BEI) for the Fe/BTS artificially tilted multilayer block. It can be seen that the Fe/BTS artificially tilted multilayer block grows into a three-layer interfacial structure, which consists of Fe layer in the left side with a black color, interface reaction layer in the middle region with a dark gray color and BTS layer in the right side with a light gray color. The enlarged BEI images further manifest that there are three distinctive regions from the Fe layer to the BTS layer (Figure 5b). The Fe and BTS maintain excellent interface bonding, and no crack on the micrometer scale is observed. To figure out the composition of the three regions, we performed an energy-dispersive spectrometer (EDS) analysis (Figure 5c–e), and the corresponding average atomic ratios of Fe, Bi, Te and Se on the zones are listed in Table 2. The black area was confirmed to be Fe. The light gray area is $Bi_2Te_{2.69}Se_{0.20}$, indicating a small amount of loss of Te and Se during the preparation of Fe/BTS ATMTD. The dark gray area in the middle region is speculated to be FeTe and Fe(Se, Te), which results from the interfacial reaction between Fe and BTS.

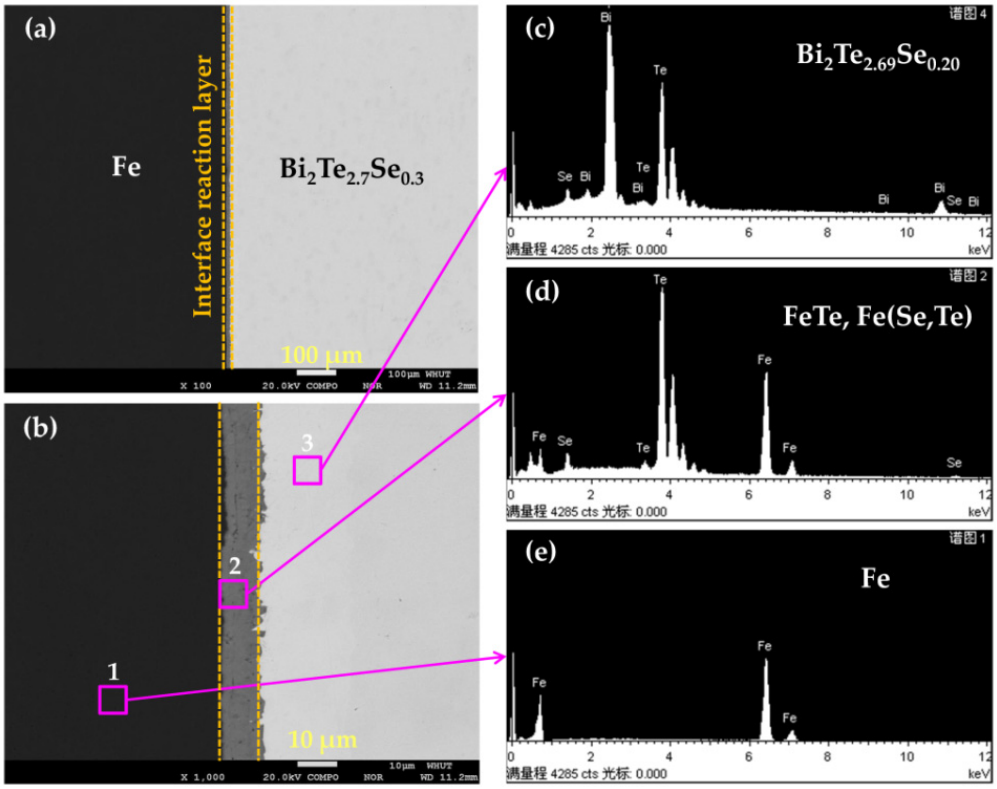


**Figure 5.** (**a**,**b**) BEI; (**c**,**d**,**e**) EDS results of Fe/BTS artificially tilted multilayer block.

**Table 2.** EDS results and speculated compositions of the different zones in Figure 5.

| Zones | Atomic Ratio (%) | | | | Speculated Composition |
|---|---|---|---|---|---|
| | Fe | Bi | Te | Se | |
| Fe | 100 | 0 | 0 | 0 | Fe |
| | 53.04 | 0 | 43.25 | 3.71 | FeTe, Fe(Se, Te) |
| BTS | 0 | 40.95 | 55.01 | 4.04 | $Bi_2Te_{2.69}Se_{0.20}$ |

The BEI and line distributions of Fe, Bi, Te and Se elements were also conducted on the Fe/BTS interface by a wave-dispersive spectrometer (WDS), as shown in Figure 6. It is clear that three-layer interfacial structure is present from the Fe to BTS sides. The line distributions show that all the elements have a small amount of diffusion at the interface. However, the thickness of interface reaction layer is only 8 μm, which means that the interfacial reaction between Fe and BTS is slight, SPS and two-step WEDM method is suitable for fabricating a high-quality Fe/BTS ATMTD.

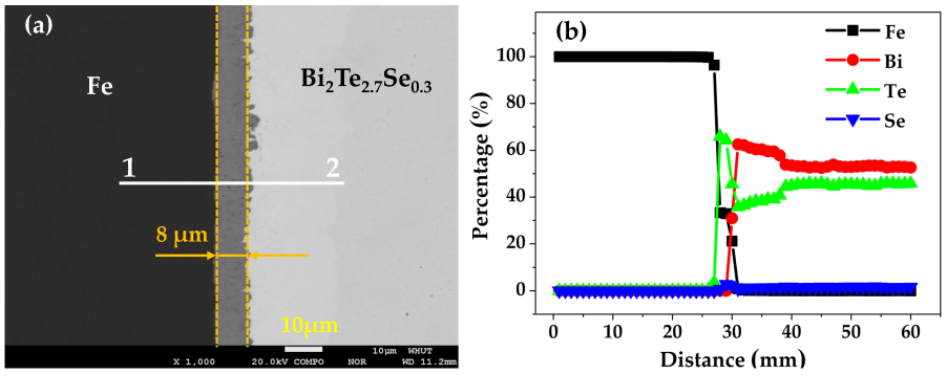


**Figure 6.** (**a**) BEI; (**b**) elemental line profiles of Fe, Bi, Te and Se elements at the Fe/BTS interface.

### *3.3. Power Generation Performance of Fe/BTS ATMTD*

Prior to recording the power-generation performance, a V–I measurement was performed for the packaged Fe/BTS ATMTD at a fixed ΔT of 20 K in the self-made measuring equipment (Figure 7). The inset shows the differences from reliability tests. The deviation within 5% indicates a good reproducible behavior in self-made measuring equipment.

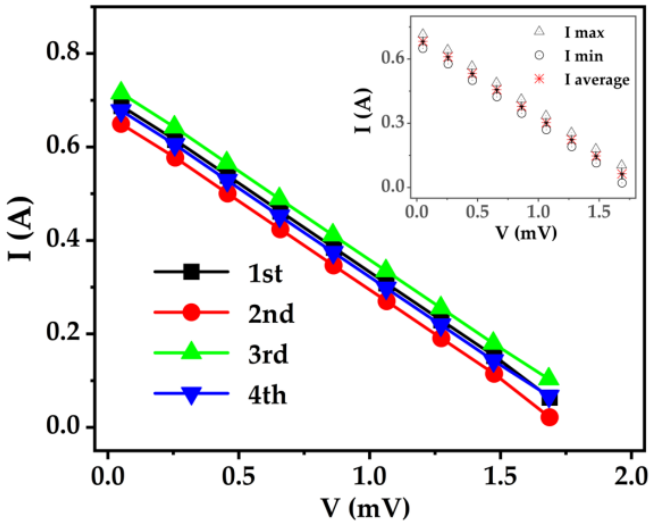


**Figure 7.** V–I curve of Fe/BTS ATMTTD at a fixed ΔT of 20 K after being testing four times. The inset shows the differences with the self-made measuring equipment.

To characterize the power generation performance of the as-prepared Fe/BTS ATMTD, the electrical output characteristics were evaluated with the self-made measurement system under various $\Delta T_z$ values. The theoretical $\Delta V_x$ values were estimated according to the equation $\Delta V_x = S_{zx}\Delta T_z l/h$, where $S_{zx}$ is the transverse Seebeck coefficient of the as-prepared Fe/BTS ATMTD, l is the length of the as-prepared Fe/BTS ATMTD, h is the height of the as-prepared Fe/BTS ATMTD and $\Delta T_z$ is the temperature difference along the z direction. It can be seen that a $\Delta V_x$ along the x direction has generated when a $\Delta T_z$ applies along the z direction, clearly demonstrating the transverse Seebeck effect (Figure 8a). The experimental $S_{zx}$ is 27 μV/K, which is within error to the theoretical ones of 30 μV/K [34]. The $\Delta V_x$ gradually increases with increasing the $\Delta T_z$. When $\Delta T_z$ = 9.4 K or 42.2 K, a maximum $\Delta V_x$ value is up to 0.7 mV and 3.4 mV, respectively. It may be noted that the $\Delta V_x$ value of over 7 V might be achieved in micro-scaled Fe/BTS ATMTD with h of 4 μm, l of 120 mm and $\Delta T_z$ of 9.4 K. The work voltage (V) and output power (P) as a function of work current (I) for Fe/BTS ATMTD under different ΔT are depicted in Figure 8b. The linear relationship of V and the parabolic variation of P as a function of I represents a typical feature of TE power generators, where the slope of V–I mean the internal resistance of Fe/BTS ATMTD. When the external resistance is matched with internal resistance, a peak P can be reached. The peak P of 0.20 mW is obtained under a TH of 293.4 K and ΔT of 9.4 K, and it increases with increasing ΔT. The maximum P is 3.87 mW for Fe/BTS ATMTD under TH of 324.0 K and ΔT of 39.6 K. The related power density per heat-transfer area is 53.75 $W \cdot m^{-2}$.

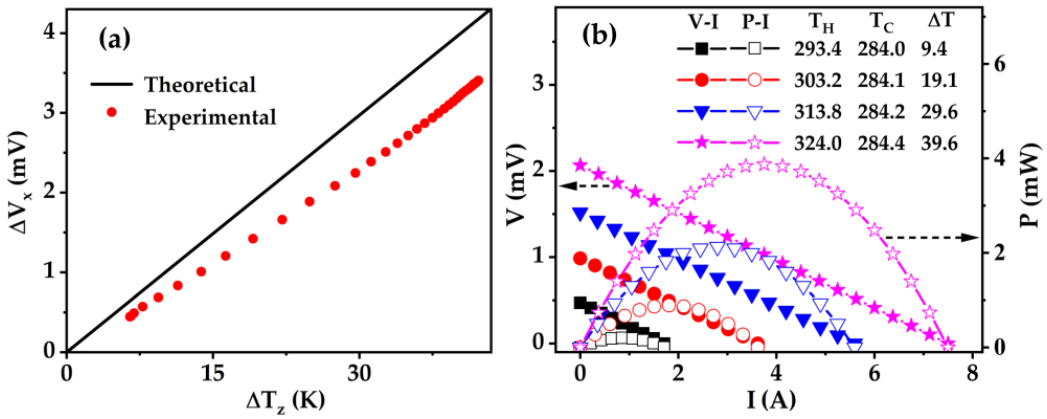


**Figure 8.** Power-generation performance of Fe/BTS ATMTTD: (**a**) $\Delta T_z$ dependence of $\Delta V_x$; (**b**) I dependences of V and P for Fe/BTS ATMTD.

## 4. Conclusions

A high-throughput calculation was developed to rationally design the geometrical configuration of high-performance Fe/BTS ATMTD. It was revealed that the Fe/BTS ATMTD exhibits a maximum $ZTz_x$ of 0.15 when δ = 0.49 and θ =14°. According to the optimized δ and θ, a Fe/BTS ATMTD of 12 mm in length, 6 mm in width and 4 mm in height was fabricated via the SPS and two-step WEDM method. Our microstructure analysis showed that the whole Fe/BTS interface is closely connected with a slight interfacial reaction. The thickness of interface reaction layer is only 8 μm. The maximum $\Delta V_x$ value is up to 0.7 mV and 3.4 mV when $\Delta T_z$ = 9.4 K and 42.2 K, respectively. The Fe/BTS ATMTD achieved a maximum P of up to 3.87 mW under a ΔT of 39.6 K, and the related power density per heat-transfer area reached 53.75 $W \cdot m^{-2}$. In the future, the performance of Fe/BTS ATMTD will be further improved if the height of the device is in the order of micron. This work demonstrates the versatile application of Fe/BTS ATMTD in power generation.

**Author Contributions:** Software, data curation, writing—original draft preparation, funding acquisition, H.Z.; methodology, investigation, H.L.; writing—review and editing, formal analysis, G.Q.; writing—review and editing, validation, H.Y., X.G. and X.L.; conceptualization, visualization, J.Z. All authors have read and agreed to the published version of the manuscript.

**Funding:** This work was support by the National Natural Science Foundation of China (52008043, 51778071), the Hunan Province Natural Science Foundation of China (2020JJ5598), the China Postdoctoral Science Foundation (2019M652747, 2020T130570) and the Open Fund (kfj190105) of National Engineering Laboratory of Highway Maintenance Technology (Changsha University of Science and Technology).

**Acknowledgments:** EPMA experiments were performed at the Center for Materials Research and Testing of Wuhan University of Technology. Transverse thermoelectric performance measurements were performed at State Key Laboratory of Advanced Technology for Materials Synthesis and Processing of Wuhan University of Technology. The authors are grateful to X.L. Nie, W.T. Zhu, W.Y. Zhao and P. Wei from Wuhan University of Technology for their fruitful collaborations.

**Conflicts of Interest:** The authors declare no conflict of interest.

## References

1. Ren, W.; Sun, Y.; Zhao, D.L.; Aili, A.; Shi, C.Q.; Zhang, J.L.; Geng, H.Y.; Zhang, J.; Zhang, L.X.; Xiao, J.L.; et al. High-performance wearable thermoelectric generator with self-healing, recycling, and lego-like reconfiguring capabilities. *Sci. Adv.* **2021**, *7*, eabe0586. [CrossRef] [PubMed]
2. Mao, J.; Chen, G.; Ren, Z.F. Thermoelectric cooling materials. *Nat. Mater.* **2021**, *20*, 454–461. [CrossRef] [PubMed]
3. Kotov, M.A.; Shemyakin, A.N.; Solovyov, N.G.; Solovyova, N.G.; Yakimov, M.Y.; Glebov, V.N.; Dubrova, G.A.; Malyutin, A.M.; Popov, P.A.; Poniaev, S.A.; et al. Performance assessment of thermoelectric detector for heat flux measurement behind a reflected shock of low intensity. *Appl. Therm. Eng.* **2021**, *195*, 117143. [CrossRef]
4. Md Aspan, R.; Fatima, N.; Mohamed, R.; Syafiq, U.; Ibrahim, M.A. An overview of the strategies for tin selenide advancement in thermoelectric application. *Micromachines* **2021**, *12*, 1463. [CrossRef] [PubMed]
5. Xie, G.Z.; Li, Z.; Luo, T.T.; Bai, H.; Sun, J.C.; Xiao, Y.; Zhao, L.D.; Wu, J.S.; Tan, G.J.; Tang, X.F. Band inversion induced multiple electronic valleys for high thermoelectric performance of SnTe with strong lattice softening. *Nano Energy* **2020**, *69*, 104395. [CrossRef]
6. Sidharth, D.; Nedunchezhian, A.S.A.; Akilan, R.; Srivastava, A.; Srinivasan, B.; Immanuel, P.; Rajkumar, R.; Devi, N.Y.; Arivanandhan, M.; Liu, C.J.; et al. Enhanced thermoelectric performance of band structure engineered $GeSe_{1-x}Te_x$ alloys. *Sustain. Energy Fuels* **2021**, *5*, 1734–1746. [CrossRef]
7. Feng, B.; Jiang, X.X.; Pan, Z.; Hu, L.; Hu, X.M.; Liu, P.H.; Ren, Y.; Li, G.Q.; Li, Y.W.; Fan, X.A. Preparation, Structure, and enhanced thermoelectric properties of Sm-doped BiCuSeO oxyselenide. *Mater. Des.* **2020**, *185*, 108263. [CrossRef]
8. Masrura, H.M.; Kareekunnan, A.; Liu, F.; Ramaraj, S.G.; Ellrott, G.; Hammam, A.M.M.; Muruganathan, M.; Mizuta, H. Design of graphene phononic crystals for heat phonon engineering. *Micromachines* **2020**, *11*, 655. [CrossRef]
9. Xiao, Y.; Zhao, L.D. Charge and phonon transport in PbTe-based thermoelectric materials. *NPJ Quantum Mater.* **2018**, *3*, 1–12. [CrossRef]
10. An, D.C.; Chen, S.P.; Zhai, X.; Yu, Y.; Fan, W.H.; Zhang, T.T.; Liu, Y.Q.; Wu, Y.C.; Wang, W.X.; Snyder, G.J. High-performance p-type elemental Te thermoelectric materials enabled by the synergy of carrier tuning and phonon engineering. *J. Mater. Chem. A* **2020**, *8*, 12156–12168. [CrossRef]
11. Zhang, Z.X.; Zhao, K.P.; Wei, T.R.; Qiu, P.F. $Cu_2Se$-Based liquid-like thermoelectric materials: Looking back and stepping forward. *Energy Environ. Sci.* **2020**, *13*, 3307–3329. [CrossRef]
12. Gayner, C.; Amouyal, Y. Energy filtering of charge carriers: Current trends, challenges, and prospects for thermoelectric materials. *Adv. Funct. Mater.* **2020**, *30*, 1901789. [CrossRef]
13. Zhao, W.Y.; Liu, Z.Y.; Sun, Z.G.; Zhang, Q.J.; Wei, P.; Mu, X.; Zhou, H.Y.; Li, C.C.; Ma, S.F.; He, D.Q.; et al. Superparamagnetic enhancement of thermoelectric performance. *Nature* **2017**, *549*, 247–251. [CrossRef]
14. Jaziri, N.; Boughamoura, A.; Müller, J.; Mezghani, B.; Tounsi, F.; Ismail, M. A comprehensive review of Thermoelectric Generators: Technologies and common applications. *Energy Rep.* **2020**, *6*, 264–287. [CrossRef]
15. Shi, X.L.; Zou, J.; Chen, Z.G. Advanced thermoelectric design: From materials and structures to devices. *Chem. Rev.* **2020**, *120*, 7399–7515. [CrossRef] [PubMed]
16. Zhou, W.N.; Yamamoto, K.; Miura, A.; Iguchi, R.; Miura, Y.; Uchida, K.; Sakuraba, Y. Seebeck-driven transverse thermoelectric generation. *Nat. Mater.* **2021**, *20*, 463–467. [CrossRef]
17. Scudder, M.R.; He, B.; Wang, Y.X.; Rai, A.; Cahill, D.G.; Windl, W.; Heremans, J.P.; Goldberger, J.E. Highly efficient transverse thermoelectric devices with $Re_4Si_7$ crystals. *Energy Environ. Sci.* **2021**, *14*, 4009–4017. [CrossRef]
18. Sakai, A.; Minami, S.; Koretsune, T.; Chen, T.; Higo, T.; Wang, Y.M.; Nomoto, T.; Hirayama, M.; Miwa, S.; Nishio-Hamane, D.; et al. Iron-based binary ferromagnets for transverse thermoelectric conversion. *Nature* **2020**, *581*, 53–57. [CrossRef]

19. Reimann, T.; Bochmann, A.; Vogel, A.; Capraro, B.; Teichert, S.; Töpfer, J. Fabrication of a transversal multilayer thermoelectric generator with substituted calcium manganite. *J. Am. Ceram. Soc.* **2017**, *100*, 5700–5708. [CrossRef]
20. Li, Y.Z.; Wei, P.; Zhou, H.Y.; Mu, X.; Zhu, W.T.; Nie, X.L.; Sang, X.H.; Zhao, W.Y. Geometrical structure optimization design of high-performance $Bi_2Te_3$-based artificially tilted multilayer thermoelectric devices. *J. Electron. Mater.* **2020**, *49*, 5980–5988. [CrossRef]
21. Yu, W.Y.; Yan, G.Y.; Xue, Y.L.; Zhang, Y.J.; Wang, J.L.; Fu, G.S.; Wang, A.F. Enhanced light-induced transverse thermoelectric effect in tilted BiCuSeO film via the ultra-thin AuNPs layer. *Nanoscale Res. Lett.* **2019**, *14*, 1–6. [CrossRef] [PubMed]
22. Razeghi, M. *InAs/GaSb Type II Superlattices: A Developing Material System for Third Generation of IR Imaging: Mid-Infrared Optoelectronics*; Woodhead Publishing: Cambridge, MA, USA, 2020; pp. 379–413. [CrossRef]
23. Gamino, M.; Santos, J.G.S.; Souza, A.L.R.; Melo, A.S.; Della Pace, R.D.; Silva, E.F.; Oliveira, A.B.; Rodríguez-Suárez, R.L.; Bohn, F.; Correa, M.A. Longitudinal spin Seebeck effect and anomalous Nernst effect in CoFeB/non-magnetic metal bilayers. *J. Magn. Magn. Mater.* **2021**, *527*, 167778. [CrossRef]
24. Mu, X.; Zhu, W.T.; Zhao, W.Y.; Zhou, H.Y.; Sun, Z.G.; Li, C.C.; Ma, S.F.; Wei, P.; Nie, X.L.; Yang, J.H.; et al. Excellent transverse power generation and cooling performances of artificially tilted thermoelectric film devices. *Nano Energy* **2019**, *66*, 104145. [CrossRef]
25. Goldsmid, H.J. Porous materials in synthetic transverse thermoelements. *J. Electron. Mater.* **2010**, *39*, 1987–1989. [CrossRef]
26. Tang, Y.; Cui, B.Y.; Zhou, C.L.; Grayson, M. p × n-type transverse thermoelectrics: A novel type of thermal management material. *J. Electron. Mater.* **2015**, *44*, 2095–2104. [CrossRef]
27. Qian, B.; Ren, F. Cooling performance of transverse thermoelectric devices. *Int. J. Heat Mass Tran.* **2016**, *95*, 787–794. [CrossRef]
28. Kyarad, A.; Lengfellner, H. Al-Si multilayers: A synthetic material with large thermoelectric anisotropy. *Appl. Phys. Lett.* **2004**, *85*, 5613–5615. [CrossRef]
29. Kanno, T.; Yotsuhashi, S.; Sakai, A.; Takahashi, K.; Adachi, H. Enhancement of transverse thermoelectric power factor in tilted Bi/Cu multilayer. *Appl. Phys. Lett.* **2009**, *94*, 061917. [CrossRef]
30. Reitmaier, C.; Walther, F.; Lengfellner, H. Power generation by the transverse Seebeck effect in Pb-$Bi_2Te_3$ multilayers. *Appl. Phys. A* **2011**, *105*, 347–349. [CrossRef]
31. Kanno, T.; Sakai, A.; Takahashi, K.; Omote, A.; Adachi, H.; Yamada, Y. Tailoring effective thermoelectric tensors and high-density power generation in a tubular $Bi_{0.5}Sb_{1.5}Te_3$/Ni composite with cylindrical anisotropy. *Appl. Phys. Lett.* **2012**, *101*, 011906. [CrossRef]
32. Sakai, A.; Kanno, T.; Takahashi, K.; Tamaki, H.; Kusada, H.; Yamada, Y.; Abe, H. Breaking the trade-off between thermal and electrical conductivities in the thermoelectric material of an artificially tilted multilayer. *Sci. Rep.-UK* **2014**, *4*, 1–6. [CrossRef] [PubMed]
33. Zhu, W.Y.; Guo, X.G.; Sang, X.H.; Wei, P.; Nie, X.L.; Zhao, W.Y.; Zhang, Q.J. Fabrication and performance prediction of Ni/$Bi_{0.5}Sb_{1.5}Te_3$ artificially-tilted multilayer devices with transverse thermoelectric effect. *J. Power Sources* **2021**, *512*, 230471. [CrossRef]
34. Mu, X.; Zhou, H.Y.; Zhao, W.Y.; He, D.Q.; Zhu, W.T.; Nie, X.L.; Sun, Z.G.; Zhang, Q.J. High-performance $YbAl_3$/$Bi_{0.5}Sb_{1.5}Te_3$ artificially tilted multilayer thermoelectric devices via material genome engineering method. *J. Power Sources* **2019**, *430*, 193–200. [CrossRef]
35. Soleimani, Z.; Zoras, S.; Ceranic, D.B.; Shahzad, S.; Cui, Y.L. A review on recent developments of thermoelectric materials for room-temperature applications. *Sustain. Energy. Technol.* **2020**, *37*, 100604. [CrossRef]
36. Goldsmid, H.J. Application of the transverse thermoelectric effects. *J. Electron. Mater.* **2011**, *40*, 1254–1259. [CrossRef]
37. Da Rosa, A.V.; Ordonez, J.C. *Fundamentals of Renewable Energy Processes*, 4th ed.; Katey Birtcher: Cambridge, MA, USA, 2021; pp. 220–226. [CrossRef]